Author/s:
Nath, SK;Syed, N;Pan, W;Yu, Y;Liu, D;Nielsen, MP;Yuwono, J;Kumar, PV;Zhu, Y;Cortie, DL;Nguyen, CK;Fu, L;Roberts, A;Faraone, L;Ekins-Daukes, NJ;Lei, W

Title:
Liquid Metal-Exfoliated SnO2-Based Mixed-Dimensional Heterostructures for Visible-to-Near-Infrared Photodetection

Date:
2025

Citation:
Nath, S. K., Syed, N., Pan, W., Yu, Y., Liu, D., Nielsen, M. P., Yuwono, J., Kumar, P. V., Zhu, Y., Cortie, D. L., Nguyen, C. K., Fu, L., Roberts, A., Faraone, L., Ekins-Daukes, N. J. & Lei, W. (2025). Liquid Metal-Exfoliated SnO2-Based Mixed-Dimensional Heterostructures for Visible-to-Near-Infrared Photodetection. Advanced Optical Materials, 13 (25), https://doi.org/10.1002/adom.202500765.

Persistent Link:
https://hdl.handle.net/11343/357235

RESEARCH ARTICLE

ADVANCED OPTICAL MATERIALS
www.advopticalmat.de

# Liquid Metal-Exfoliated $SnO_2$-Based Mixed-Dimensional Heterostructures for Visible-to-Near-Infrared Photodetection

*Shimul Kanti Nath,* Nitu Syed,* Wenwu Pan, Yang Yu, Dawei Liu, Michael P. Nielsen, Jodie Yuwono, Priyank V. Kumar, Yan Zhu, David L. Cortie, Chung K. Nguyen, Lan Fu, Ann Roberts, Lorenzo Faraone, Nicholas J. Ekins-Daukes, and Wen Lei*

**Ultra-thin 2D materials have gain significant attention for making next-generation optoelectronic devices. Here, a large-area heterojunction photodetector is fabricated using a liquid metal-printed 2D $SnO_2$ layer transferred onto CdTe thin films. The resulting device demonstrates efficient broadband light sensing from visible to near-infrared wavelengths, with enhanced detectivity and faster photo response. Significantly, the device shows a $\approx 10^5$-fold increase in current than the dark current level when illuminated with a 780 nm laser and achieves a specific detectivity of $\approx 10^{12}$ Jones, nearly two orders of magnitude higher than that of a standalone CdTe device. Additionally, temperature-dependent optoelectronic testing shows that the device maintains a stable response up to 140 °C and generates distinctive photocurrent at temperatures up to 80 °C, demonstrating its thermal stability. Through band structure analysis, DFT calculations, and photocurrent mapping, the formation of a p-n junction is confirmed, which enhances carrier separation via the built-in potential, significantly boosting photoresponse. These results highlight the potential of liquid metal-derived 2D materials in heterostructure integration, paving the way for advanced optoelectronic applications.**

## 1. Introduction

2D materials have attracted significant recent attention for their use in optoelectronics owing to their extraordinary properties emerging from ultra-thin, atomic-scale architecture[1–3] In particular, 2D layers of metal oxides have emerged as promising candidates for their use in next-generation photodetectors[4] which have applications in a variety of areas, including telecommunications, scientific instrumentation, astronomy, surveillance, and defense.[5–7] However, the nanoscale thickness of these materials poses a significant limitation, as it permits the absorption of only a minimal portion of the incident light, thereby constraining their efficacy in light-driven applications, particularly within the visible to near-infrared (NIR) spectral range.[8] Developing innovative strategies that enhance light-matter

S. K. Nath, M. P. Nielsen, Y. Zhu, N. J. Ekins-Daukes
School of Photovoltaic and Renewable Energy Engineering
University of New South Wales (UNSW Sydney)
Kensington, NSW 2052, Australia
E-mail: shimul_kanti.nath@unsw.edu.au

S. K. Nath, W. Pan, L. Faraone, W. Lei
Australian Research Council Centre of Excellence for Transformative Meta-Optical Systems
Department of Electrical
Electronic and Computer Engineering
The University of Western Australia
35 Stirling Highway, Perth, WA 6009, Australia

N. Syed, C. K. Nguyen
School of Engineering
RMIT University
Melbourne, VIC 3001, Australia
E-mail: nitu.syed@rmit.edu.au

The ORCID identification number(s) for the author(s) of this article can be found under https://doi.org/10.1002/adom.202500765



**DOI: 10.1002/adom.202500765**

N. Syed, A. Roberts
Australian Research Council Centre of Excellence for Transformative Meta-Optical Systems
School of Physics
University of Melbourne
Victoria 3010, Australia

Y. Yu, D. Liu, L. Fu
Australian Research Council Centre of Excellence for Transformative Meta-Optical Systems
Department of Electronic Materials Engineering
Research School of Physics
The Australian National University
Canberra ACT 2601, Australia

D. Liu
Institute of Applied Physics
Abbe Center of Photonics
Friedrich Schiller University Jena
Albert-Einstein-Straße 15, 07745 Jena, Germany

J. Yuwono
School of Chemical Engineering
The University of Adelaide
Adelaide, SA 5005, Australia

P. V. Kumar
School of Chemical Engineering
University of New South Wales (UNSW Sydney)
Kensington, NSW 2052, Australia

interactions is crucial to harness their potential fully. Constructing mixed-dimensional (2D/3D) heterostructures is of particular interest because they provide several advantages, including enhanced light absorption, a broad spectral range (UV to IR), formation of built-in potential, which assists in separating photo-generated carriers leading to fast photo-response, and extended functionality such as self-powered photodetection. These attributes are useful in environments that require ultralow power consumption, a small device footprint, and wireless operation.[9,10] Therefore, significant efforts have been made to develop heterostructures incorporating new 2D materials with high sensitivity, wide detection ranges, rapid response times, and ease of fabrication.[11–13]

To date, the majority of p-n heterojunction-based photodetectors have concentrated on combinations such as silicon with graphene[14] or transition metal dichalcogenides (TMDCs), including $MoS_2$,[15,16] while more recently, a limited number of studies have investigated graphene paired with GaN[17] and SnS/graphene hybrid system.[18] Importantly, heterojunctions involving non-layered 2D metal oxides (such as $SnO_2$) combined with 3D semiconductors remain less explored, highlighting a promising and under-investigated area of research. The dangling bonds on the surface of non-layered 2D metal oxides exhibit high chemical activity, providing enhanced opportunities to tailor their chemical reactivity with other materials.[19]

The growth and characterization of 2D material-based heterostructure devices are challenging due to the difficulty of growing large-area 2D layers on appropriate substrates. Recently, liquid metal-based synthesis techniques have been developed that offers an effective means of realizing various 2D metal oxides and compounds due to the relative simplicity of the synthesis process.[20–22] Due to the high surface tension, the surface of liquid metals is often described as atomically flat, providing an optimal environment for creating ultrathin 2D materials following the Cabrera–Mott oxidation process.[20,21,23] In addition, the liquid metal-based exfoliation method overcomes critical limitations of conventional techniques for the synthesis of 2D metal oxides. Unlike chemical vapor deposition (CVD), which suffers from small-area uniformity issues and grain boundary defects[24,25] or molecular beam epitaxy (MBE) requiring ultra-high vacuum and slow growth rates,[26] the liquid metal synthesis approach enables rapid, ambient-condition production of wafer-scale 2D nanosheets. Moreover, liquid metal-based printing techniques facilitate synthesizing a wide range of materials, including naturally stratified, non-layered compounds, significantly expanding the available family of 2D materials. However, incorporating liquid metal-derived semiconducting oxides as a mixed heterostructure platform has rarely been reported and has remained an active area of research. Such a hybrid system could offer tuneable band alignments, exceptional optical properties, and atomically smooth interfaces, enabling efficient charge dynamics and broadband light responsiveness.

Tin dioxide ($SnO_2$) has emerged as a critical material in various optoelectronic and sensing applications, including solar cells (as an electron transport layer),[27] ultraviolet (UV) photodetectors,[28] and diverse sensors.[29–31] This versatility is attributed to its desirable properties, such as high chemical stability, a wide bandgap (3.4 to 4 eV), and superior electron mobility.[32–35] Recent research highlights its potential in UV photodetection, particularly when $SnO_2$ is combined with other materials, making heterostructures, such as $SnO_2/MoS_2$,[36] $SnO_2$/halide perovskites[37] and $SnO_2$-NiO.[38] On the other hand, cadmium telluride (CdTe) is also a technologically important material that exhibits promising optoelectronic properties, including a direct bandgap of ≈1.5 eV and a high optical absorption coefficient that enables effective light absorption above the bandgap, making it an excellent candidate for photodetector and solar cell applications.[39–42] The favorable band alignment of these two materials and the excellent electron transport properties of $SnO_2$ could offer significant potential for further applications.[43,44] However, no report exists on heterostructure photodetectors integrating non-layered 2D $SnO_2$ with CdTe technology.

This study uses the liquid metal synthesis technique to fabricate a heterostructure-based photodetector utilizing 2D $SnO_2$ layers transferred onto bulk CdTe thin films. This mixed-dimensional photodetector exhibits enhanced broadband light detection and outperforms conventional CdTe photodetectors by offering higher detectivity and a faster photoresponse. These advances highlight the significant benefits and potential of incorporating liquid metal-exfoliated ultrathin materials into next-generation nano-optoelectronic devices.

## 2. Results and Discussion

### 2.1. Material Synthesis and Characterisation

**Figure 1a** shows a schematic of the liquid metal synthesis technique used to produce centimetre-scale ultra-thin tin oxide ($SnO_x$) layers.[45] This single-step liquid metal printing technique involves exfoliating 2D $SnO_x$ from freshly preconditioned tin melted at 280 °C in an ambient atmosphere (further details are given in the experimental section). Under these conditions, the resulting $SnO_x$ comprises a mixture of tin monoxide (SnO) and tin dioxide ($SnO_2$).[31,45] Post-transfer annealing in ambient air was performed to promote the $SnO_2$ phase, yielding near-uniform 2D nanosheets, as shown in Figure 1b–d. An optical image of the 2D $SnO_2$ layer transferred onto a CdTe thin film of ≈5 µm thickness is shown in Figure 1b, and an AFM image of the structure is shown in Figure 1c, identifying a $SnO_2$ thickness of ≈2 nm with minimal surface roughness. The average surface roughness of the CdTe and $SnO_2$ was ≈0.23 and 0.18 nm, respectively. Further characterization of the $SnO_2$, including the cross-sectional HRTEM images of $SnO_2$/CdTe interface has been provided in Figure S1 (Supporting Information). Figure 1d shows a photoluminescence image of a 2D $SnO_2$

D. L. Cortie
Australian Centre for Neutron Scattering
Australian Nuclear Science and Technology Organisation
Lucas Heights, NSW 2234, Australia
C. K. Nguyen
School of Chemical and Biomolecular Engineering
University of Sydney
Darlington, New South Wales 2008, Australia

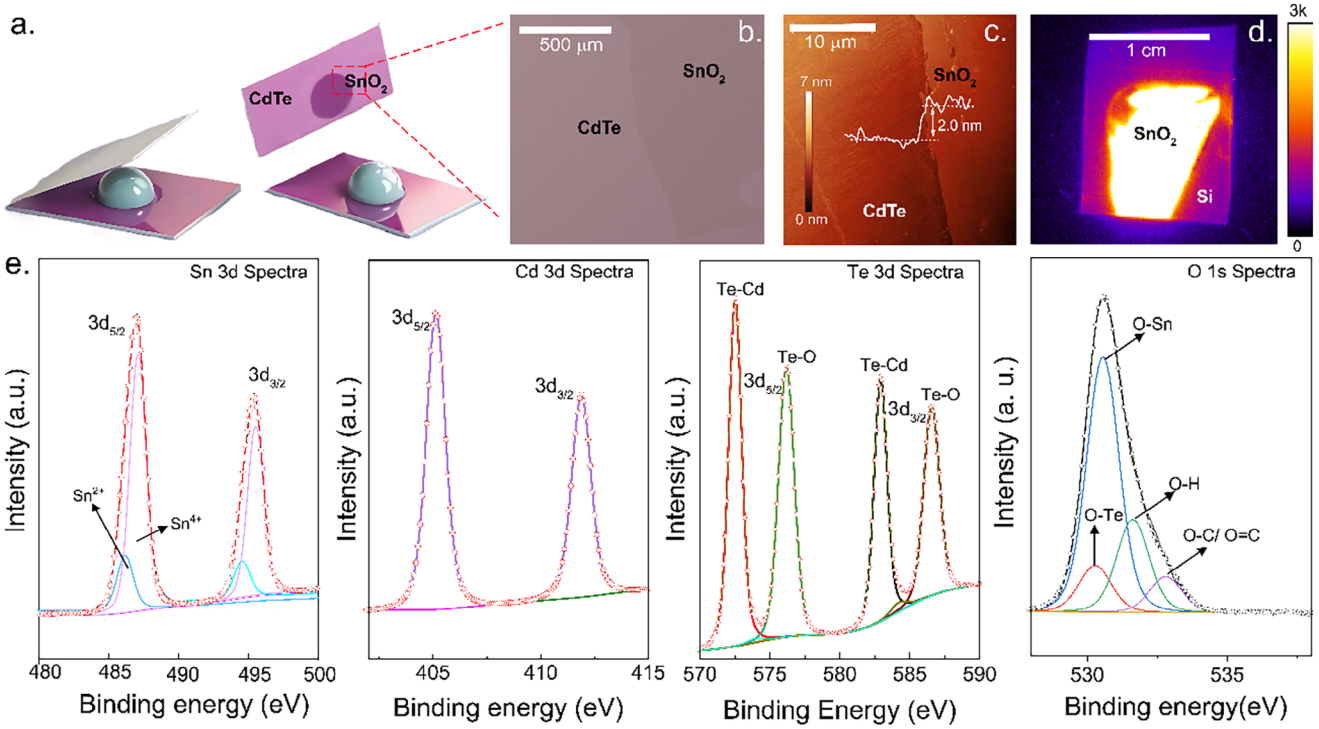


**Figure 1.** a) Schematic of the liquid metal synthesis technique, b) optical image showing the exfoliated $SnO_2$ onto the CdTe thin film, c) AFM image confirming the thickness of the as-deposited 2D $SnO_2$ layer, d) photoluminescence image of a 2D $SnO_2$ transferred onto a Si substrate showing the overall cm-scale growth of $SnO_2$ and e) XPS spectra of $SnO_2$/CdTe heterostructure.

layer produced by the same process but transferred onto a bare Si substrate, demonstrating the compatibility of the synthesis method across various substrates. Here, $SnO_2$ on Si serves as a surface passivation layer, enabling visualization of the quality and yield of the large-area ultrathin layer obtained through this technique.

The chemical states of the $SnO_2$/CdTe interface were analyzed using X-ray photoelectron spectroscopy (XPS), with the resulting spectra for Sn 3d, Cd 3d, Te 3d, and O 1s shown in Figure 1e. The XPS analysis reveals the presence of $Sn^{4+}$ and $Sn^{2+}$, with the dominant response resulting from the presence of the $SnO_2$ phase. The dominance of the $SnO_2$ phase is also supported by Raman measurements (Figure S1c, Supporting Information) and thermodynamic considerations (see Supporting Information). The XPS data showed no detectable $Sn^0$ peak and maintained Sn $3d_5/_2$ peaks at characteristic binding energies (≈486.9 eV for $Sn^{4+}$ and ≈485.7 eV for $Sn^{2+}$),[45] verifying the stoichiometry during the heterojunction preparation. The deconvolution of Sn 3d XPS spectra (Figure 1e) revealed a predominant $Sn^{4+}$ oxidation state (82.9%), confirming $SnO_2$ as the primary phase, along with a minor $Sn^{2+}$ component (17.1%). Note that the device fabrication using photolithography involved subjecting the materials to multiple brief annealing steps in air, water rinsing, and atmospheric storage with no encapsulation before electrical measurements. This processing potentially affects Sn oxidation states, with $SnO_2$ likely prevailing under these conditions.[31,46,47] Additionally, the XPS data indicate Te oxidation (formation of $TeO_2$ and $TeO_x$)[48] at the surface, consistent with observations seen in Te-terminated CdTe grown by molecular beam epitaxy (see Figure S2, Supporting Information). The O 1s spectrum shows peaks associated with various oxygen species for the $SnO_2$-CdTe heterostructure. The optical absorbance spectra of $SnO_2$, presented in Figure S3a (Supporting Information), exhibit a pronounced absorption peak in the UV region, with no significant absorption at wavelengths above 400 nm, consistent with the previous reports.[49] As shown in Figure S3b (Supporting Information), CdTe thin film exhibited absorption within the UV to visible range (up to 821 nm, corresponding to its optical bandgap), as reported by previous litertaure.[50]

### 2.2. Photodetection Performance

A two-terminal photodetector partly incorporating the uncovered CdTe thin film and the $SnO_2$/CdTe heterostructure, as shown in **Figure 2a**, was fabricated. The device response was investigated under illumination with lasers of different wavelengths. As shown in Figure 2b,c, illumination of the whole device area between the two electrodes significantly influenced the device response with increased device current. The data show that the device exhibits sensitivity across a wide wavelength range, from the visible to the near-infrared region. The photocurrent, defined as the difference between the laser on and off currents ($I_{Ph} = I_{laser\ on} - I_{laser\ off}$), was found to increase with the increase of bias voltage (Figure 2c) within the visible-to-NIR wavelengths, as expected. Consistent photocurrent and dark current levels across photoswitching cycles (i.e., laser on and off cycles) confirm a stable photo response to incident light.

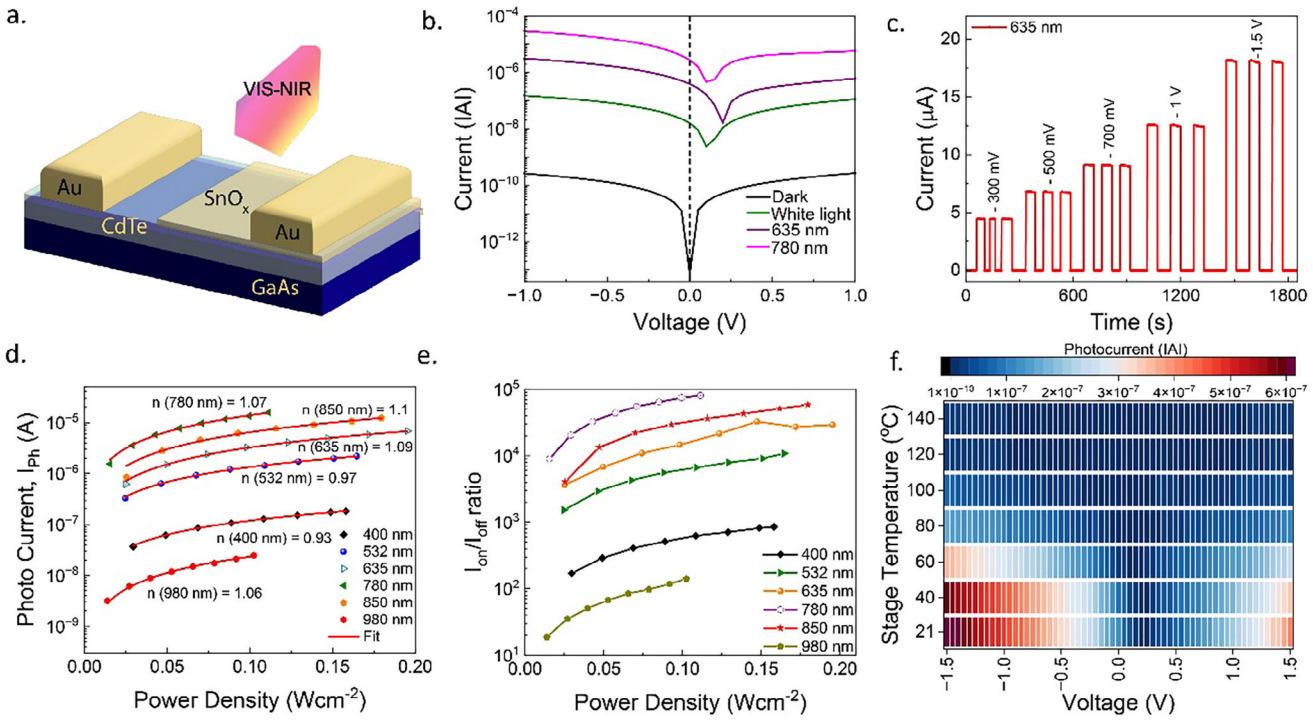


**Figure 2.** a) Schematic of the device structure, b) quasi-static *I–V* characteristics upon illumination with different laser and white light sources, and c) Light-induced increase of device current as a function of voltage bias with 60 s light ON/OFF time at an illumination with a 635 nm laser, d,e) Photocurrent and $I_{on/off}$ ratio as a function of wavelength and power density, respectively, and f) temperature-dependent photocurrents (measured with a laser of 850 nm wavelength and power density ≈ 263 mW cm$^{-2}$) when the device was heated at elevated stage temperatures.

Figure 2d,e show the light-intensity-dependent photo response of the device under varying laser wavelengths and power densities. The photocurrent increases with laser power (Figure 2d), following a power-law relationship, $I_{Ph} \propto P^n$, where "P" is the power density and "n" is the power index. Across all tested wavelengths, "n" deviates slightly from unity, ranging from 0.93 at 400 to 1.1 at 850 nm. This deviation is attributed to non-radiative carrier recombination mediated by defect states at shorter wavelengths (400 and 532 nm), as described in previous studies.[51,52] At longer wavelengths (635, 780, 850, and 980 nm), the observed deviation is likely due to photothermal heating,[53] which facilitates carrier generation through electron emission from trap states under increased photon flux density, a parameter directly proportional to the wavelength.

Importantly, the device demonstrated a high $I_{on}/I_{off}$ ratio, exhibiting a ≈$10^5$-fold increase in current upon illumination with a 780 nm laser at a power density of 100 mW cm$^{-2}$ (Figure 2e), clearly identifying its potential for high-sensitivity/low-noise device applications. The device reliability was further tested by varying the stage temperature and recording the photocurrent by illuminating the device with an 850 nm laser, as shown in Figure 2f. The figure demonstrates that the device maintained a distinctive photo response up to 80 °C and continued to exhibit photo response at an elevated temperature of 140 °C, albeit with a 30-fold reduction (measured at −1.5 V) compared to room temperature, indicating excellent performance in harsh environments. The bias polarity-dependent photocurrent is discussed in Section 2.3.

Responsivity and specific detectivity were further evaluated and benchmarked against a CdTe device without the $SnO_2$ layer. Measurements under six distinct laser illuminations revealed that, for constant laser power density (100 mW cm$^{-2}$), the device responsivity increased by nearly an order of magnitude, while the specific detectivity improved by two orders of magnitude (see **Figure** 3a,b). The photocurrent data are given in (Figure S4, Supporting Information).

Device response was also assessed under broadband illumination (420–1000 nm) using an 888-W tungsten-halogen lamp with measurements taken at each wavelength at 5 nm intervals to investigate the detailed spectral photo response. The photocurrent data, presented in Figure 3c, indicates enhanced sensitivity in the heterostructure, with a 5 nm resolution in wavelength. It is evident that while the CdTe device demonstrated optimal sensitivity near its bandgap (821 nm), the heterostructure displayed that within a broader wavelength range, such as between 500 and 940 nm.

To assess the response speed of the fabricated photodetectors under various illumination conditions, measurements of rise and fall times were performed, as summarized in Figure 3d–f. Figure 3d illustrates a representative dynamic photo response curve, defining rise and fall times as the periods required for the current to increase from 10% to 90% of its peak value and decrease from 90% to 10%, respectively. These measurements offer critical insights into the dynamic performance of our device. $SnO_2$/CdTe heterostructures and CdTe-only devices exhibit characteristic response times within the millisecond range, with the

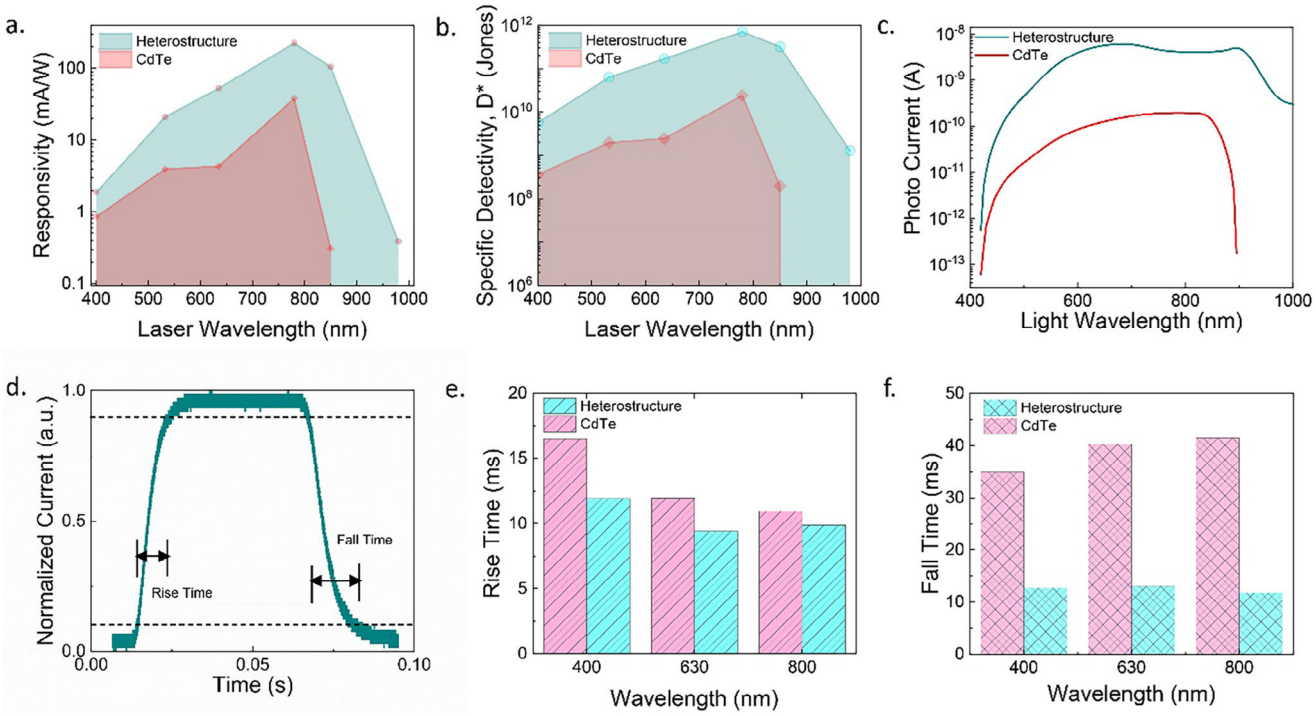


**Figure 3.** Comparison of a,b) responsivity and specific detectivity ($D^*$) for devices based on $SnO_2$/CdTe heterostructures and CdTe alone (The responsivity ($R$) of the photoconductor was defined as $R = I_{Ph}/P.S$, where P is the incident power intensity of the laser beam, and S is the active device area. $D^*$calculated using the relation: $D^* = I_{Ph}.\sqrt{S}/\ (P.S.\sqrt{2q.I_{dark}})$.[54] This measurement used lasers of 6 distinct wavelengths with 100 mW $cm^{-2}$ power density. c) Photocurrent (measured at a bias voltage of −1 V) as a function of wavelength measured using a tungsten-halogen lamp by measuring photocurrent at each wavelength with a 5 nm interval d) Dynamic photo response curve and e,f) Extracted photo response times (rise and fall times, respectively) for $SnO_2$/CdTe heterostructures and CdTe-only devices when illuminated with different laser wavelengths.

heterostructure exhibiting a faster response irrespective of laser wavelengths, as summarised in Figure 3e,f. We also tested the photo response characteristics of devices with varying electrode gaps and employed CdTe substrates with different orientations. All the devices exhibited reliable photo responses, as shown in Figure S5 (Supporting Information).

**Table 1** summarizes the key performance metrics of our device, along with recently reported photodetectors based on 2D materials, $SnO_2$, CdTe, and their heterostructures in bulk or thin film form. While direct comparisons are limited due to variations in device sizes, dimensions, choice of electrode metals, and operating conditions, the fabricated photodetectors exhibit a notable

**Table 1.** Comparison of photodetection performance of different heterostructures.

| Material | Wavelength range/Peak response | Bias voltage | $I_{on}/Io_{ff}$ ratio | Laser power [mW $cm^{-2}$] | Specific detectivity [Jones] | Rise time/Fall time [ms] | Refs. |
|---|---|---|---|---|---|---|---|
| CdTe/CdS Core-shell nanostructure | 510 nm | −7.5 V | – | – | $4.5 \times 10^{11}$ | – | [55] |
| $CdTe/MoS_2$ | 405 nm | 0 V | – | 0.0739 | $5.84 \times 10^{11}$ | 0.044/0.13 | [56] |
| CdTe nanosheets | 473 nm | 1 V | 27 | 132.3 | $10^9$ | 18.4/14.7 | [57] |
| $MoS_2$/Si | 450-1000 nm | 0.5 V | | 25 | $2 \times 10^{11}$ @ 580 nm | 0.01/0.019 | [15] |
| Graphene/GaN | 360 nm | 1.5 V | | 0.095 | $1 \times 10^{17}$ | 0.35/0.36 | [17] |
| $Sb_2Se_3$ thin films | 940 nm | 5 V | 31 | – | $8.58 \times 10^{10}$ | 35/38 | [58] |
| $PdSe_2$ thin films | 730 nm | 0 V | – | – | $5.17 \times 10^{11}$ | 0.72/0.24 | [59] |
| GaSe/$VO_2$ | 405 nm | 3 V | 433 | 150.10 | $2.14 \times 10^{11}$ | | [60] |
| FTO/$CdTe_{1-x}Se_x$/CdTe | 443 nm | −1 V | – | | $2.6 \times 10^7$ | 22/21 | [61] |
| $SnO_2$/CdTe | 400-980 nm | 0.5 V | $\approx 10^5$ @ 780 nm | 100 | $0.72 \times 10^{12}$ @ 780 nm | 9.8/11.7 @ 800 nm | This work* |

*The performance of the heterostructure and CdTe devices were compared using a 780 nm laser wavelength, as it was the closest available wavelength to the bandgap of CdTe due to the unavailability of 821 nm lasers in our lab

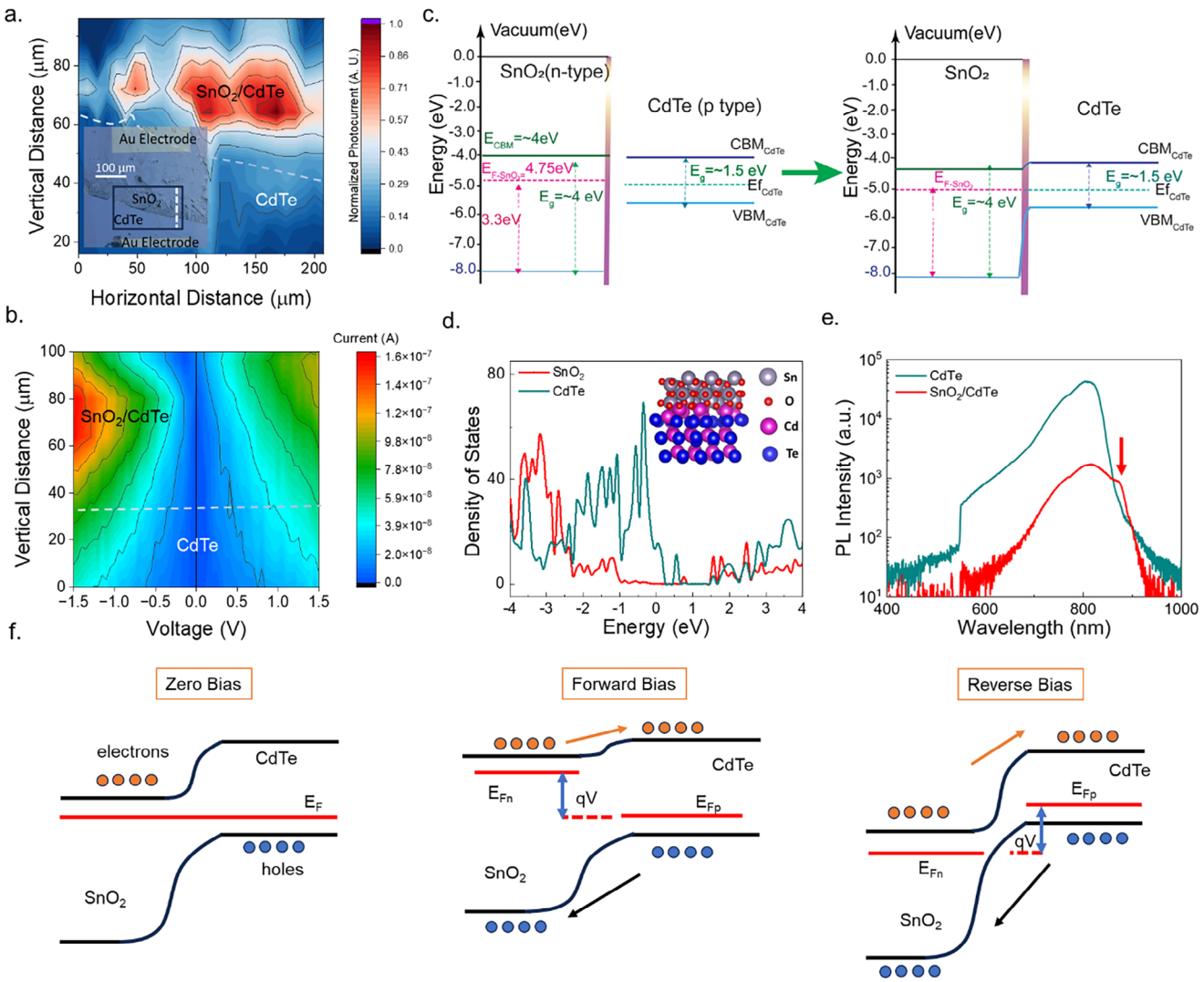


**Figure 4.** a) 2D photocurrent map of the selected device area marked by the rectangle in the inset showing an optical microscope image of the whole device area (Laser power was 0.6 μW at 700nm during photocurrent mapping); the white dashed line shows the boundary between device regions with $SnO_2$/CdTe and CdTe only and b) photo-gated quasi-static *I–V* along the straight line shown inset of (a). Additional photocurrent as a function of bias voltage for the $SnO_2$/CdTe heterostructure and CdTe regions are shown in Figure S6 (Supporting Information) c) Schematic band diagrams of individual materials (experimental) and their heterostructure (expected), d) Density of states as a function of energy calculated by DFT, e) PL spectra of CdTe and $SnO_2$/CdTe heterostructure without applying any bias, and f) schematics showing the electronic transport under different bias conditions (V is the magnitude of applied bias; the other notations have their usual meaning as described in a typical p-n junction).

enhancement in photocurrent and a broadband photo response, demonstrating their competitiveness.

It is important to highlight that the reported figures of merit, including responsivity, specific detectivity, and the response time of our photodetector, are affected by the photoconductive uncoated CdTe and material inhomogeneity. These parameters could be further optimized by employing photolithographically defined selective area etching of $SnO_2$ to reduce the uncoated CdTe region and access the underlying CdTe layer for one of the electrode depositions. Additionally, scaling down the overall device area could enhance specific detectivity as it scales with area,[62] and minimizing parasitic contributions from the measurement circuit may also improve device performance, such as response speed.

### 2.3. Mechanism of the Enhanced Photoresponse

To investigate the enhanced photo response of the heterostructure device, a photocurrent map was recorded by applying a 1V bias voltage and illuminating the device with a 700 nm laser. **Figure** 4a shows the photocurrent map of the selected device area, identifying that both CdTe and the $SnO_2$/CdTe heterostructure contribute to the overall photocurrent response, with a dominant contribution from the heterostructure. A line scan was also conducted under illumination along the direction shown in Figure 4a (indicated by the dashed straight line in the optical image), and quasi-static *I–V* curves were recorded along the line, which provides additional insight (Figure 4b). In this configuration, the device exhibited forward-bias

characteristics when a negative bias was applied to the electrode directly in contact with the $SnO_2$ layer and reverse-bias characteristics when a positive bias was applied to the same electrode. Under negative bias, photocurrent is generated across the entire scanned area, with the active region concentrating on the $SnO_2$/CdTe region. Importantly, the $SnO_2$/CdTe region exhibited more significant bias-polarity-dependent current asymmetry than the CdTe region, indicative of junction formation within this area (Figure 4b). In this context, it is worth noting that the dark current characteristics also exhibit polarity-dependent current asymmetry (Figure 2b), suggesting a complex current transport mechanism within the device structure. Despite this complexity, the photocurrent mapping distinctly reveals contributions from both the CdTe region and the $SnO_2$/CdTe heterostructure, with the latter demonstrating a dominant photocurrent response.

To elucidate the nature of the junction formed in the heterostructure, we further investigated the band structure, combining the results of different techniques, such as valence band XPS (VB-XPS), photoemission spectroscopy in the air (PESA), photoluminescence, and UV–vis spectroscopy. The experimental data from these measurements are provided in (Figures S7 and S8, Supporting Information), and simplified band diagrams of the individual materials and that of the heterostructure are shown in Figure 4c. Our analysis identified that the liquid metal synthesis technique achieved n-type $SnO_2$ with an optical bandgap of≈ 4 eV and a Fermi level at ≈ −4.75 eV, consistent with the dominance of the $SnO_2$ phase in the nanosheet. In contrast, p-type CdTe with a bandgap of ≈1.5 eV and Fermi level at ≈ −5 eV was achieved by Molecular Beam Epitaxy, consistent with previous reports.[63–65] Consequently, a vertical p-n junction with a type-II band alignment[66] was formed when the two materials were hetero-integrated, notably without extrinsic doping. The p-type conductivity of undoped CdTe is related to the intrinsic Cd vacancy,[63–65] and the n-type nature of $SnO_2$ is due to embedded oxygen vacancy or defects introduced by the synthesis technique.[67]

The band alignment at the heterojunction strongly affects the charge transport across the interface and hence the overall optoelectronic response of the device, and was further studied by density functional theory (DFT) calculations. Figure 4d shows the DFT calculated electronic band structure, which is consistent with experimental findings, i.e., $SnO_2$ presents a large bandgap of ≈4 eV (VBM ≈−2.5 eV and CBM ≈1.5 eV), and CdTe presents a smaller bandgap of ≈1.5 eV (VBM around the Fermi level and CBM ≈1.5 eV). The valence band maximum of $SnO_2$ lies well below the Fermi level, while that of CdTe is positioned closer to it. In contrast, the conduction band minimum for CdTe and $SnO_2$ appears relatively similar above the Fermi level, consistent with the anticipated band alignment at the heterostructure interface (the partial density of states is given in Figure S9, Supporting Information).

Significantly, DFT analysis shows that several defect/hybridization states arise within the bandgaps due to defect/hybridization states arising from the interface coupling, further indicated by the results of PL measurements, as shown in Figure 4e. Under excitation with a 532 nm laser, the $SnO_2$/CdTe structure exhibits a distinct emission peak at ≈880 nm (as indicated by the arrow), alongside the dominant 820 nm peak associated with the direct bandgap energy of CdTe (1.5 eV). Electron-hole pairs generated at the conduction band-valence band edges could relax into these states at the interface, thus lowering their energy before recombination, which could enhance the broadband photocurrent.

The above analyses offer valuable insights into the enhanced photo response of the heterostructure device, which can be elucidated through the energy band diagrams presented in Figure 4f. Under zero-bias conditions, most photogenerated electron-hole pairs are created within the CdTe layer, benefiting from its optimal bandgap. The built-in electric field at the CdTe/$SnO_2$ heterojunction effectively drives electrons toward the $SnO_2$ layer and holes toward the CdTe layer, facilitating carrier separation and reducing recombination losses. When a negative bias is applied to the *n*-type $SnO_2$, the barrier height for electrons in the $SnO_2$ is lowered, allowing electrons to traverse the junction more readily, as shown in Figure 4f, enhancing current generation. Conversely, applying a positive bias to *n*-type $SnO_2$ increases the potential barrier, suppressing current generation. The high electron mobility of the liquid metal-derived ultrathin $SnO_2$ (Figure S10, Supporting Information) could also support efficient photogenerated carrier collection, while its wide bandgap prevents holes from reaching the electrode, ensuring unidirectional current flow and further improving the photocurrent. The type-II band alignment in the heterostructure broadens its absorption spectrum due to band bending, enabling the capture of photons over a wider wavelength range. This generates more charge carriers and significantly improves the photo response, as evident from Figure 3a,b. It is also noteworthy to highlight the contribution of photocurrent generated by photogenerated carriers in the CdTe layer (uncovered by $SnO_2$) that diffuse to the heterojunction and are collected by the built-in electric field. These carriers contribute to both the photocurrent and the dark current, potentially reducing the device speed. Overall, the enhanced photo response of the $SnO_2$/CdTe heterostructure is achieved through efficient charge transport, reduced recombination, and broadened spectral sensitivity. The distinct electrical conductivities, favorable band alignment, and high electron transfer efficiency of the $SnO_2$ layer facilitate these advantages.

## 3. Conclusion

In summary, we demonstrated the integration of liquid metal-printed ultrathin $SnO_2$ nanosheets onto CdTe thin films and unlocked a broadband-sensitive photodetector with a response from the visible to the near-infrared spectra. The device exhibited efficient generation of photocurrents, achieving a maximum current on/off ratio of ≈$10^5$ under 100 mW $cm^{-2}$ power density of a 780 nm laser, a responsivity of 233 $mAW^{-1}$, and a specific detectivity of ≈$10^{12}$ Jones, nearly two orders of magnitude higher than that of devices fabricated with pure CdTe thin films. Additionally, the device generated photocurrents at elevated temperatures up to 140 °C (with efficient photo response up to 80 °C), highlighting its robust thermal stability. Compared to a pure CdTe device, which is mostly responsive to wavelengths near its bandgap (820 nm), the heterostructure displayed excellent optical sensitivity within a broader wavelength range, such as between 500 and 940 nm. Furthermore, the heterostructure demonstrated faster response times than the CdTe-only device, independent of the

illumination wavelength. The enhanced performance of the heterostructure was attributed to the formation of a *p-n* junction, which occurs without external doping, as confirmed by band structure analysis, DFT calculations, and photocurrent mapping. Moreover, this study presents a reproducible and scalable fabrication approach for developing next-generation nanoscale photodetectors and optoelectronic devices tailored for broadband applications.

## 4. Experimental Section

*Synthesis of 2D $SnO_2$*: 2D $SnO_2$ layers were exfoliated from the oxidized surface of liquid tin under an ambient environment by following the liquid metal synthesis technique. At first, elemental tin (purity 99.99%) purchased from Roto Metal was melted at a substrate temperature of 280 °C. The melted metal was compressed between two glass slides to eliminate pre-existing oxide layers and potential airborne contaminants. Following this preparation, the newly formed oxide skin was gently detached by touching the surface with a pre-heated substrate (Si, $SiO_2$, and CdTe grown on GaAs) at 280 °C (see Figure 1a). The prepared nanosheets were then post-annealed at 450 °C for 15 min under ambient air conditions to achieve the dominant $SnO_2$ phase.[31] The CdTe thin films were grown using the molecular beam epitaxy (MBE) technique, as described in our earlier studies,[67,68] and the structural, optical, and compositional properties are given in (Figures S2,S3, Supporting Information).

*Material Characterization*: The structural properties of the samples were characterized using a Rigaku SmartLab X-ray diffractometer equipped with Cu K$\alpha$ radiation at a wavelength of 1.5406 Å. The instrument was operated at 40 kV and 40 mA, with an angular scanning range of $10° \leq 2\theta \leq 90°$ to capture fundamental diffraction peaks. Layer thicknesses and compositional analysis were analyzed using Bruker Dimension Icon AFM operating under ScanAsyst-air mode and a Thermo Scientific monochromatic Al K$\alpha$ XPS spectrometer (h$\nu$ ≈1486.6 eV) equipped with a concentric hemispherical analyzer, respectively. The XPS data was processed using CasaXPS software. TEM images were taken using a JEOL JEM-2100F TEM operating at an acceleration voltage of 200 kV equipped with a Gatan OneView camera. Gatan Microscopy suite software was utilized to analyze the data. TEM samples were prepared by directly printing the tin oxide sheets onto thermally and mechanically robust silicon nitride membrane window grids ($Si_3N_4$ grids, Ted Pella, 21587-10). Raman spectra of the synthesized and annealed 2D $SnO_x$ were carried out using a Raman spectrometer (Horiba Scientific LabRAM HR Evolution) equipped with a 532 nm laser source and 1800 $mm^{-1}$ grating. PESA Riken Keiki AC-2 was utilized to study the band structure of different samples at a power of 500 nW. The optical absorbance spectra of $SnO_2$ nanosheets and CdTe thin films were acquired using a UV–vis Carry spectrophotometer.

*Device Fabrication and Testing*: The ultrathin $SnO_2$-based photodetectors were fabricated using a direct writing photolithography process. First, AZ 5214E photoresist was spin-coated onto 2D tin oxide sheets deposited on MBE-grown CdTe thin films. The wafers were soft-baked on a hot plate at 95 °C for 90 s. The electrodes were patterned using a Maskless Aligner (Heidelberg MLA150). The samples were developed in AZ-726 MIF developer after laser writing. An e-beam evaporator (PVD75 – Kurt J. Lesker) was then employed to deposit Cr/Au (10/100 nm) electrodes, followed by a lift-off process defining a 250 µm × 250 µm active device area.

Electrical and optoelectronic measurements were performed using a Keysight B2902A Precision source unit, a Keithley 4200SCS semiconductor parameter analyzer, and an Agilent 2912A source meter. All the measurements were performed in the air, and biases were applied to the electrode deposited directly on top of 2D $SnO_2$ while the electrode deposited directly on top of CdTe was grounded. To assess the effects of light exposure, devices were subjected to laser illumination from sources with wavelengths of 400, 532, 630, 635, 700, 780, 850, and 980 nm, as well as to broadband light from a broadband 888-Watt Tungsten Halogen Lamp (Newport Model 66886). A SpectraPro 2300i monochromator was used to control the wavelength of incident light. The laser illumination covered the entire device area during the measurement, with the spot diameter ≈250 µm. The photocurrent mapping was performed using a WhiteLase SC400 High-Power Supercontinuum laser with a circular spot diameter of 10 µm. A WiTec alpha300 S scanning near optical microscope (SNOM) was used to locate the laser spot on the device and adjust the three-axial stage moving step. Illumination power was calibrated using a Thorlabs power meter, and the photo response dynamics were recorded using a WaveAce 102, 60 MHz Oscilloscope.

*DFT Calculations*: Density functional theory (DFT) calculations of the band structure were performed using the Projector Augmented Wave (PAW) method[69,70] as implemented in the Vienna Ab initio Simulation Package (VASP).[71] The calculations were completed with a plane-wave cut-off energy of 500 eV and a single Gamma k-point mesh. The electronic self-consistent calculation was converged to $1 \times 10^{-5}$ eV, and ionic relaxation steps were performed using the conjugate-gradient method (IBRION = 2) and continued until the total force on each atom dropped below a tolerance of −0.05 eV $Å^{-1}$. The generalized gradient approximation (GGA) of the Perdew–Burke–Ernzerhof (PBE)approach[72] was used. Initially, the relaxation of CdTe (space group: $F\bar{4}3m$ (Cubic); lattice parameter, a: 6.6237 Å) and $SnO_2$ (space group: $P4_2/mnm$ (Tetragonal); lattice parameters, a: 4.8242 Å and c: 3.2404 Å) unit cells were conducted, followed by the optimization of the slabs of the CdTe/$SnO_2$ interface. The joint interface slab model of CdTe and $SnO_2$ was developed based on experimental observation of the oxidized CdTe surface. The band alignment investigations were further calculated using the hybrid functionals approach of Heyd–Scuseria–Ernzerhof (HSE) using the relaxed structure obtained from the PBE approach.[73]

## Supporting Information

Supporting Information is available from the Wiley Online Library or from the author.

## Acknowledgements

S.K.N. acknowledges the support from the Forrest Research Foundation in the form of the Forrest Prospect Fellowship, ARC DP220101532, and ACNS grant proposal number 17399, respectively. N. Syed recognizes the support of a Vice Chancellor Fellowship from the RMIT University and acknowledges the support from McKenzie postdoctoral fellowship. The authors acknowledge the support from TMOS CE200100010 grant and thank Dr. Renjie Gu, Songqing Zhang, Dr. Xiao Sun, Dr. Phuong Y. Le, and Dr. Mark Lockrey for assisting with CdTe growth, material and device characterization, and setting up an electrical testing unit. N.S. acknowledges the facilities and the technical assistance of RMIT University's Microscopy and Microanalysis Facility (RMMF) and Micro Nano Research Facility (MNRF).

## Conflict of Interest

The authors declare no conflict of interest.

## Data Availability Statement

The data that support the findings of this study are available in the supplementary material of this article.

## Keywords

2D, DFT, heterostructure, liquid metal, photocurrent mapping, vis–NIR photodetection

Received: March 18, 2025
Revised: June 22, 2025
Published online:

[1] J. Wang, J. Han, X. Chen, X. Wang, *Info. Mat.* **2019**, *1*, 33.
[2] B. W. Baugher, H. O. Churchill, Y. Yang, P. Jarillo-Herrero, *Nat. Nanotechnol.* **2014**, *9*, 262.
[3] S. Das, A. Sebastian, E. Pop, C. J. McClellan, A. D. Franklin, T. Grasser, T. Knobloch, Y. Illarionov, A. V. Penumatcha, J. Appenzeller, *Nat. Electron.* **2021**, *4*, 786.
[4] F. Koppens, T. Mueller, P. Avouris, A. Ferrari, M. Vitiello, M. Polini, *Nat. Nanotechnol.* **2014**, *9*, 780.
[5] W. Ahmad, J. Liu, J. Jiang, Q. Hao, D. Wu, Y. Ke, H. Gan, V. Laxmi, Z. Ouyang, F. Ouyang, *Adv. Funct. Mater.* **2021**, *31*, 2104143.
[6] S. W. Cho, C. Jo, Y.-H. Kim, S. K. Park, *Nanomicro Lett* **2022**, *14*, 203.
[7] T. Ahmed, M. Tahir, M. X. Low, Y. Ren, S. A. Tawfik, E. L. Mayes, S. Kuriakose, S. Nawaz, M. J. Spencer, H. Chen, *Adv. Mater.* **2021**, *33*, 2004207.
[8] X. Li, J. Zhu, B. Wei, *Chem. Soc. Rev.* **2016**, *45*, 3145.
[9] E. Lee, H. Yoo, *Molecules* **2021**, *26*, 5056.
[10] J. Yang, J. Li, A. Bahrami, N. Nasiri, S. Lehmann, M. O. Cichocka, S. Mukherjee, K. Nielsch, *ACS Appl. Mater. Interfaces.* **2022**, *14*, 54034.
[11] P. Vashishtha, P. Prajapat, A. Sharma, P. Singh, S. Walia, G. Gupta, *ACS Appl. Electron. Mater.* **2023**, *5*, 1891.
[12] J. Liu, Q. Hao, H. Gan, P. Li, B. Li, Y. Tu, J. Zhu, D. Qi, Y. Chai, W. Zhang, *Laser Photonics Rev.* **2022**, *16*, 2200338.
[13] L. H. Zeng, S. H. Lin, Z. J. Li, Z. X. Zhang, T. F. Zhang, C. Xie, C. H. Mak, Y. Chai, S. P. Lau, L. B. Luo, *Adv. Funct. Mater.* **2018**, *28*, 1705970.
[14] T. Cui, R. Lv, Z.-H. Huang, S. Chen, Z. Zhang, X. Gan, Y. Jia, X. Li, K. Wang, D. Wu, *J. Mater. Chem. A* **2013**, *1*, 5736.
[15] V. Dhyani, S. Das, *Sci. Rep.* **2017**, *7*, 1.
[16] G. H. Shin, J. Park, K. J. Lee, G.-B. Lee, H. B. Jeon, Y.-K. Choi, K. Yu, S.-Y. Choi, *ACS Appl. Mater. Interfaces.* **2019**, *11*, 7626.
[17] J. Li, X. Xi, S. Lin, Z. Ma, X. Li, L. Zhao, *ACS Appl. Mater. Interfaces.* **2020**, *12*, 11965.
[18] X. Li, S. Ruan, H. Zhu, *Nanomaterials* **2022**, *12*, 2777.
[19] S. Zhao, J. Zhang, L. Fu, *Adv. Mater.* **2021**, *33*, 2005544.
[20] T. Daeneke, P. Atkin, R. Orrell-Trigg, A. Zavabeti, T. Ahmed, S. Walia, M. Liu, Y. Tachibana, M. Javaid, A. D. Greentree, S. P. Russo, R. B. Kaner, K. Kalantar-Zadeh, *ACS Nano* **2017**, *11*, 10974.
[21] C. K. Nguyen, M. X. Low, A. Zavabeti, B. J. Murdoch, X. Guo, P. Aukarasereenont, A. Mazumder, A. Dubey, A. Jannat, M. A. Rahman, K. Chiang, V. K. Truong, L. Bao, C. F. McConville, S. Walia, T. Daeneke, N. Syed, *Adv. Optical Mater.* **2022**, *20*, 2200925.
[22] P. Aukarasereenont, A. Goff, C. K. Nguyen, C. F. McConville, A. Elbourne, A. Zavabeti, T. Daeneke, *Chem. Soc. Rev.* **2022**, *51*, 1253.
[23] A. Zavabeti, J. Z. Ou, B. J. Carey, N. Syed, R. Orrell-Trigg, E. L. Mayes, C. Xu, O. Kavehei, A. P. O'Mullane, R. B. Kaner, *Science* **2017**, *358*, 332.
[24] P.-C. Shen, Y. Lin, H. Wang, J.-H. Park, W. S. Leong, A.-Y. Lu, T. Palacios, J. Kong, *IEEE Trans. Electron Devices* **2018**, *65*, 4040.
[25] R. Dong, T. Zhang, X. Feng, *Chem. Rev.* **2018**, *118*, 6189.
[26] A. Zavabeti, A. Jannat, L. Zhong, A. A. Haidry, Z. Yao, J. Z. Ou, *Nanomicro Lett.* **2020**, *12*, 1.
[27] B. Du, K. He, G. Tian, X. Che, L. Song, *J. Mater. Chem. C.* **2023**, *11*, 13625.
[28] M. Kumar, A. Saravanan, S. A. Joshi, S.-C. Chen, B.-R. Huang, H. Sun, *Sens. Actuators A: Phys.* **2024**, *373*, 115441.
[29] Y. Zhang, Q. Xie, L. Lyu, J. Zou, Z. Lu, *ACS Omega* **2024**, *9*, 16055.
[30] S. Kanth, A. K. Chikara, S. Choudhury, C. Betty, IEEE Applied Sensing Conference (APSCON), IEEE, Bengaluru, India, January **2023**, 1.
[31] C. K. Nguyen, P. D. Taylor, A. Zavabeti, H. Alluhaybi, S. Almalki, X. Guo, M. Irfan, M. A. Kobaisi, S. J. Ippolito, M. J. Spencer, *Adv. Funct. Mater.* **2024**, *34*, 2309342.
[32] M. Batzill, U. Diebold, *Prog. Surf. Sci.* **2005**, *79*, 47.
[33] M. Karmaoui, A. B. Jorge, P. F. McMillan, A. E. Aliev, R. C. Pullar, J. A. Labrincha, D. M. Tobaldi, *ACS Omega* **2018**, *3*, 13227.
[34] K. G. Godinho, A. Walsh, G. W. Watson, *J. Phys. Chem. C* **2009**, *113*, 439.
[35] Y. Hu, J. Hwang, Y. Lee, P. Conlin, D. G. Schlom, S. Datta, K. Cho, *J. Appl. Phys.* **2019**, *126*, 185701.
[36] P. Augustine, K. L. Kumawat, D. K. Singh, S. B. Krupanidhi, K. K. Nanda, *Appl. Phys. Lett.* **2022**, *120*, 181106
[37] S. Wang, M. Li, C. Song, C. Zheng, J. Li, Z. Li, Y. Zhang, J. Yao, *Appl. Surf. Sci.* **2023**, *623*, 156983.
[38] M. Athira, S. Bharath, S. Angappane, *Sensors Actuat A-Phys* **2022**, *340*, 113540.
[39] R. W. Birkmire, B. E. McCandless, *Curr. Opin. Solid State Mater. Sci.* **2010**, *14*, 139.
[40] T. Nagaura, H. P. Phan, V. Malgras, T. A. Pham, H. Lim, A. Ashok, J. Kim, J. You, N. T. Nguyen, J. Na, *Angew. Chem.* **2021**, *133*, 9746.
[41] Q. Lian, X. Zhu, X. Wang, W. Bai, J. Yang, Y. Zhang, R. Qi, R. Huang, W. Hu, X. Tang, *Small* **2019**, *15*, 1900236.
[42] X. Xie, S.-Y. Kwok, Z. Lu, Y. Liu, Y. Cao, L. Luo, J. A. Zapien, I. Bello, C.-S. Lee, S.-T. Lee, *Nanoscale* **2012**, *4*, 2914.
[43] A. Sharan, M. Nardone, D. Krasikov, N. Singh, S. Lany, *Appl. Phys. Rev.* **2022**, *9*, 041411.
[44] D. L. McGott, C. L. Perkins, M. O. Reese, *Sol. RRL* **2023**, *7*, 2300074.
[45] N. Syed, C. K. Nguyen, A. Zavabeti, M. X. Low, X. Wei, V. Krishnamurthi, M. Irfan, W. S. Lee, N. M. Duong, A. T. Nguyen, *ACS Appl. Electron. Mater.* **1842**, *6*, 8599.
[46] K. Nose, A. Suzuki, N. Oda, M. Kamiko, Y. Mitsuda, *Appl. Phys. Lett.* **2014**, *104*, 091905.
[47] M. Zarrinkhameh, A. Zendehnam, S. Hosseini, N. Robatmili, M. Arabzadegan, *Bull. Mater. Sci.* **2014**, *37*, 533.
[48] A. Liu, Y.-S. Kim, M. G. Kim, Y. Reo, T. Zou, T. Choi, S. Bai, H. Zhu, Y.-Y. Noh, *Nature* **2024**, *629*, 1.
[49] S. Baco, A. Chik, F. M. Yassin, *J. Sci.* **2012**, *4*, 61.
[50] D. Wang, Y. Yang, T. Guo, X. Xiong, Y. Xie, K. Li, B. Li, M. Ghali, *Sol. Energy* **2021**, *213*, 118.
[51] H. Luo, H. Wang, S. Zhang, J. Liu, Y. Ren, C. Yuan, W. Lei, *J. Alloys Compd.* **2024**, *1008*, 176819.
[52] Q. Zhao, W. Wang, F. Carrascoso-Plana, W. Jie, T. Wang, A. Castellanos-Gomez, R. Frisenda, *Mater. Horiz.* **2020**, *7*, 252.
[53] J. Tian, L. Chen, R. Qiao, K. Xiong, W. Zhang, Y. Mao, H. Li, J. Li, *Nano Energy* **2021**, *79*, 105435.
[54] H. Wang, Z. Zhang, H. Luo, S. Zhang, W. Pan, J. Liu, Y. Ren, W. Lei, *Adv. Opt. Mater.* **2024**, *30*, 2401404.
[55] Y. K. Abdalaah, O. A. Mahmood, S. S. Shaker, R. A. Ismail, *J. Opt.* **2024**, 1.
[56] S. Yang, Y. Liu, Y. Wu, F. Guo, M. Zhang, X. Zhu, R. Xu, L. Hao, *Nanoscale* **2024**, *16*, 13932.
[57] R. Cheng, Y. Wen, L. Yin, F. Wang, F. Wang, K. Liu, T. A. Shifa, J. Li, C. Jiang, Z. Wang, *Adv. Mater.* **2017**, *29*, 1703122.
[58] X. Wen, Z. Lu, L. Valdman, G.-C. Wang, M. Washington, T.-M. Lu, *ACS Appl. Mater. Interfaces.* **2020**, *12*, 35222.
[59] X. Zhang, M. Dai, W. Deng, Y. Zhang, Q. J. Wang, *Nanophotonics* **2023**, *12*, 607.
[60] J. Zhou, M. Xie, H. Ji, A. Cui, Y. Ye, K. Jiang, L. Shang, J. Zhang, Z. Hu, J. Chu, *ACS Appl. Mater. Interfaces.* **2020**, *12*, 18674.
[61] S. Yılmaz, B. M. Başol, İ. Polat, T. Küçükömeroğlu, E. Bacaksız, *J. Mater. Sci.: Mater. Electron* **2024**, *35*, 2300.
[62] W. Pan, J. Liu, Z. Zhang, R. Gu, A. Suvorova, S. Gain, H. Wang, Z. Li, L. Fu, L. Faraone, *Nano Res.* **2022**, *15*, 368.
[63] P. Emanuelsson, P. Omling, B. Meyer, M. Wienecke, M. Schenk, *Phys. Rev. B* **1993**, *47*, 15578.
[64] S. R. Kavanagh, A. Walsh, D. O. Scanlon, *ACS Energy Lett.* **2021**, *6*, 1392.
[65] A. Lindström, S. Mirbt, B. Sanyal, M. Klintenberg, *J. Phys. D: Appl. Phys.* **2015**, *49*, 035101.

[66] J. Yang, Y. Ye, R. Yu, H. Yang, H. Qiao, Z. Huang, X. Qi, *Phys. Status Solidi A* **2024**, *221*, 2400522.
[67] R. Dangi, B. Basnet, M. Pandey, S. Bhusal, B. Budhathoki, K. Parajuli, S. K. Tiwari, B. P. Kafle, *Energies* **2023**, *16*, 2653.
[68] W. Pan, S. K. Nath, S. Ma, R. Gu, Z. Zhang, L. Fu, L. Faraone, W. Lei, *J. Appl. Phys.* **2022**, *131*, 205304.
[69] P. E. Blöchl, *Phys. Rev. B* **1994**, *50*, 17953.
[70] G. Kresse, D. Joubert, *Phys. Rev. B* **1999**, *59*, 1758.
[71] G. Kresse, J. Furthmüller, *Comput. Mater. Sci.* **1996**, *6*, 15.
[72] J. P. Perdew, K. Burke, M. Ernzerhof, *Phys. Rev. Lett.* **1996**, *77*, 3865.
[73] J. Heyd, G. E. Scuseria, M. Ernzerhof, *J. Chem. Phys.* **2003**, *118*, 8207.